Check for updates

LASER & PHOTONICS REVIEWS
www.lpr-journal.org

Anisotropic Third-Harmonic Vortex Beam Generation with Ultrathin Germanium Arsenide Fork Gratings

Jayanta Deka, Jie Gao, and Xiaodong Yang**

Optical vortices have the tremendous potential to increase data capacity by leveraging the extra degree of freedom of orbital angular momentum. On the other hand, anisotropic 2D materials are promising building blocks for future integrated polarization-sensitive photonic and optoelectronic devices. Here, highly anisotropic third-harmonic optical vortex beam generation is demonstrated with fork holograms patterned on ultrathin 2D germanium arsenide flakes. It is shown that the anisotropic nonlinear vortex beam generation can be achieved independent of the fork grating orientation with respect to the crystallographic orientation. Furthermore, 2D fork hologram is designed to generate multiple optical vortices having different topological charges with strong anisotropic responses. These results pave the way toward the advancement of 2D material-based anisotropic nonlinear optical devices for future applications in photonic integrated circuits, optical communication, and optical information processing.

1. Introduction

An optical vortex has helical phase front and doughnut-shaped intensity profile which carries orbital angular momentum (OAM) defined by the azimuthal phase dependence $e^{il\theta}$, with l known as the topological charge (TC) of the vortex beam.[1] The OAM has an unbounded value of $l\hbar$ per photon which provides an extra degree of freedom for increasing data capacity in optical communication,[2] quantum information processing,[3,4] and security.[5] Besides this, OAM beams have found other applications including optical tweezers,[6,7] optical trapping,[8] and high-resolution lithography.[9] The conventional methods of generating optical vortices by using bulky optical components such as spiral phase plates and spatial light modulators are not compatible with on-chip photonic integration. Plasmonic metasurfaces which allow arbitrary control of the phase front of an optical beam have been used to generate optical vortex beams.[10] Besides linear regime, the concept of arbitrary control of amplitude and phase has also been extended into nonlinear metasurfaces, which offers the converted frequencies as an additional degree of freedom to reshape an optical beam.[11,12] However, plasmonic metasurfaces usually suffer from low nonlinear conversion efficiency and high optical loss.

Recently, 2D materials have gained significant research interests due to their intriguing electrical, optical, mechanical, and thermal properties.[13–17] In particular, the strong and controllable optical responses of 2D materials hold great promise for on-chip photonic and optoelectronic devices. Besides linear optical response, strong second- and third-order nonlinear optical responses have been reported for different kinds of 2D materials such as transition metal dichalcogenides, graphene, GaSe, GeS, GeSe, and ReS_2 with applications in second-harmonic generation (SHG),[18–22] third-harmonic generation (THG),[23,24] four-wave mixing (FWM),[25] self-phase modulation (SPM),[26] and saturable absorption (SA),[27] as well as other 2D layered materials and their hybrid structures.[28–30] In addition, in-plane anisotropy of 2D materials provide a new degree of freedom in tailoring electrical, optical, and thermal properties. Various kinds of 2D materials such as black phosphorus (BP), GeSe, SiP, As_2S_3, ReS_2, and $SnSe_2$[31–36] have been explored to understand their strong anisotropic responses. These anisotropic 2D materials have immense potential for on-chip integration applications in polarization-sensitive photodetectors,[37] polarization sensors,[38] polarized lasers,[39] optical components,[40,41] digital inverters,[42] and anisotropic memorizers.[43] In this context, 2D germanium arsenide (GeAs) belonging to monoclinic crystal structure in C2/m space group has been demonstrated to have strong in-plane anisotropic responses which can find applications in photodetection, superconductivity and thermoelectricity.[44–46] 2D GeAs is also ambiently stable making it suitable for practical applications. Along with this, 2D GeAs has been shown to have strong anisotropic THG with the maximum achievable nonlinear conversion efficiencies in the thickness range of 40–120 nm.[47]

In this work, highly anisotropic third-harmonic (TH) optical vortex beams are generated with fork holograms patterned on ultrathin 2D GeAs flakes. The amplitude and phase information of the optical vortices are encoded in binary-amplitude GeAs fork

J. Deka, X. Yang
Department of Mechanical and Aerospace Engineering
Missouri University of Science and Technology
Rolla, MO 65409, USA
E-mail: yangxia@mst.edu
J. Gao
Department of Mechanical Engineering
Stony Brook University
Stony Brook, NY 11794, USA
E-mail: jie.gao.5@stonybrook.edu

The ORCID identification number(s) for the author(s) of this article can be found under https://doi.org/10.1002/lpor.202401519

DOI: 10.1002/lpor.202401519

 © 2025 Wiley-VCH GmbH

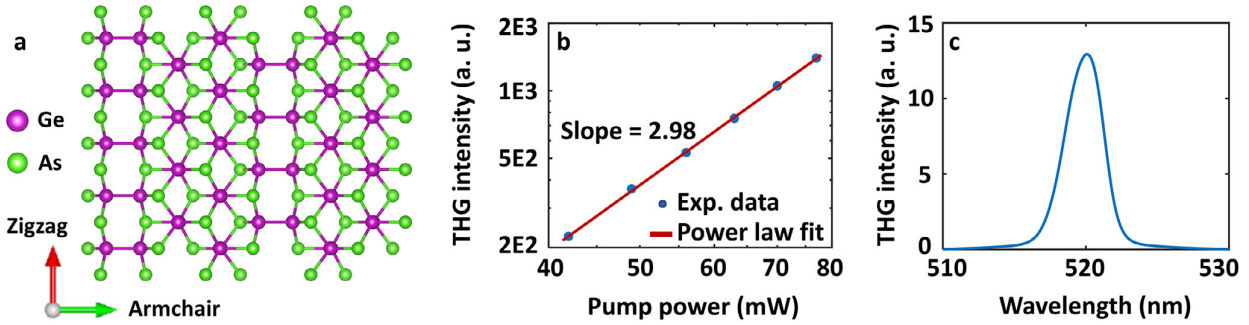

Figure 1. a) Top view of the in-plane lattice structure of 2D GeAs crystal. b) Excitation power dependence of the THG signal plotted in a log–log scale. c) Measured THG spectrum under the excitation at 1560 nm.

holograms and the generated optical vortex beams are recorded in TH far-field diffraction images. Strong anisotropic responses of the generated TH optical vortices are characterized by rotating the linear polarization of the fundamental beam. It is shown that the vortex beam with a defined topological charge can be produced with 1D fork gratings. The anisotropic nonlinear vortex beam generation is achieved independent of the fork grating orientation with respect to the GeAs crystallographic orientation. Furthermore, 2D fork hologram is used to generate multiple optical vortices having different topological charges with strong anisotropic responses. The demonstrated results offer new opportunities in advancing 2D material-based anisotropic nonlinear optical devices for future applications in photonic integrated circuits, optical communication, and optical information processing.

2. Results and Discussion

The top view of the in-plane lattice structure of an individual GeAs layer is illustrated in **Figure 1**a, which shows that GeAs has low in-plane crystal symmetry with distinguished armchair and zigzag directions. The multilayer GeAs is formed by stacking individual layers via weak van der Waals forces. This type of low-symmetry lattice structure corresponding to two different Ge-Ge bonds along armchair and zigzag directions indicates strong in-plane anisotropic optical responses in 2D GeAs crystal. For 2D GeAs crystal with monoclinic lattice structure in the space group of C2/m, the total intensity of the emitted THG signal can be represented as[47]

$$I^{3\omega} \propto \left(\chi_{11}^{(3)} cos^3\theta + 3\chi_{18}^{(3)} cos\theta sin^2\theta\right)^2 + \left(\chi_{22}^{(3)} sin^3\theta + 3\chi_{29}^{(3)} sin\theta cos^2\theta\right)^2 \quad (1)$$

where $\chi_{im}^{(3)}$ is the third-order nonlinear susceptibility tensor, θ is the excitation polarization angle of the fundamental beam with respect to the armchair axis of the crystal, and the excitation direction is perpendicular to the lattice plane illustrated in Figure 1a. The THG emission process from GeAs crystal is first confirmed by measuring the excitation power and wavelength dependences of the THG signal generated from a GeAs flake with the thickness of 91 nm transferred on a glass substrate. The transmitted THG signal from the flake is measured using a 1560 nm pump laser and a combination of a 900 nm shortpass filter and a 520 nm bandpass filter. Figure 1b plots the measured THG output signal as a function of the input pump power in a log-log scale. The cubic power law fitting with a slope of 2.98 confirms the THG process in GeAs crystal. The wavelength dependence of the emitted THG signal is plotted in Figure 1c, showing an emission peak at 520 nm which is exactly one-third of the excitation wavelength of 1560 nm.

The fork holograms are designed to imprint the amplitude and phase information of optical vortices on the 2D GeAs crystal to generate TH optical vortex beams of TC = l in the far field. The one-dimensional fork gratings are directly milled in the 2D GeAs crystal with the binary amplitude modulation of the third-order nonlinear susceptibility given by

$$\chi^{(3)}(x,y) = \chi^{(3)}\left\{\frac{1}{2} + \frac{1}{2}sgn\left[\cos\left\{\frac{2\pi x}{\Lambda} - \phi(x,y)\right\} - \cos\left\{\sin^{-1}A(x,y)\right\}\right]\right\} \quad (2)$$

where Λ is the grating period for diffraction, $\phi(x,y)$ and $A(x,y)$ are the phase and amplitude profiles of the beam wavefront in the hologram plane. The phase profile for producing TH optical vortex beam of TC = l is

$$\phi(x,y) = \begin{cases} l \cdot \tan^{-1}(y/x) & x \geq 0 \\ l \cdot \left[\tan^{-1}(y/x) + \pi\right] & x < 0 \end{cases} \quad (3)$$

and the amplitude profile $A(x,y) = 1$. The generated TH vortex beam appears in the first diffraction order with the diffraction angle determined by the THG wavelength and the grating period as $\theta_{THG} = \sin^{-1}(\lambda_{THG}/\Lambda)$. The binary-amplitude fork holograms are fabricated using focused ion beam (FIB) milling of the GeAs thin flakes transferred on glass substrates. The grating period is chosen to be $\Lambda = 2.4$ μm and the total FIB patterning area is 20×20 μm^2. **Figure 2**a,b shows the optical transmission microscope image and the scanning electron microscope (SEM) image of the fabricated fork hologram to generate TH optical vortices with TC = ±1 in the first diffraction order, with the grating lines aligned with the armchair axis. The armchair axis is identified from the polarization-dependent THG measurements of the bare GeAs flake with the direction of the maximum THG intensity corresponding to the armchair axis.[47] From the atomic force

© 2025 Wiley-VCH GmbH

18638899, 2025, 7, Downloaded from https://onlinelibrary.wiley.com/doi/10.1002/lpor.202401519 by Stony Brook University Libraries, Wiley Online Library on [02/07/2025]. See the Terms and Conditions (https://onlinelibrary.wiley.com/terms-and-conditions) on Wiley Online Library for rules of use; OA articles are governed by the applicable Creative Commons License

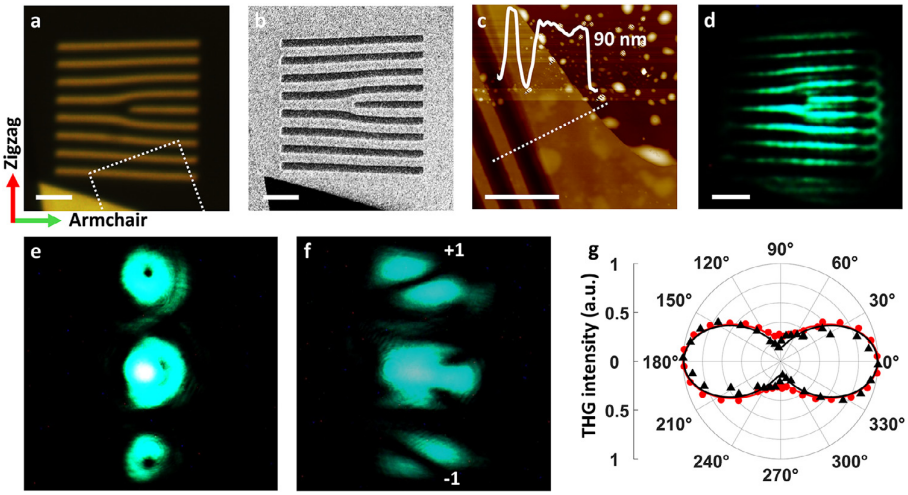

Figure 2. Anisotropic TH optical vortex generation with TC = ±1 for the grating lines aligned with the armchair axis. a) Optical transmission microscope image, b) SEM image, and c) AFM image of the fork hologram. The AFM line profile is scanned along the dotted line. The broken square in a) shows the AFM scanning area. A portion of the AFM image is outside the field of view of the optical image. d) TH image of the hologram under 1560 nm excitation. All scale bars are 5 μm. e) Far-field image of the hologram showing the generation of TH vortex beam in the first diffraction order. f) Cylindrical lens transformed image illustrating TC = ±1 for the generated optical vortices. g) Polarization angle dependence of the THG intensity of optical vortices (black triangles) and the THG intensity from the bare GeAs flake (red dots). Solid curves are the corresponding theoretical fittings.

microscopy (AFM) image and the line profile drawn across the flake shown in Figure 2c, the thickness of the GeAs flake is estimated to be 90 nm. The AFM line profile also reveals that the flake has been completely etched between the grating lines during the FIB process. Figure 2d shows the TH image of the hologram obtained under the excitation of 1560 nm pump beam linearly polarized along the armchair axis. The corresponding far-field TH image obtained in a Fourier microscopy setup is shown in Figure 2e, which shows the generation of TH optical vortices with TC = ±1 in the first diffraction order with the diffraction angle θ_{THG} of 12.6°. The TCs of the generated optical vortices are also characterized by the astigmatic transformation of the far-field images using a cylindrical lens, where the number of dark stripes determines the TC value and the stripe orientation determines its sign. The transformed image shown in Figure 2f confirms TC = ±1 for the produced TH optical vortices. Subsequently, the anisotropic THG response of the generated optical vortices is characterized by rotating the excitation linear polarization with a half-wave plate. Figure 2g plots the measured THG intensity of optical vortices depending on the polarization angle of pump beam, as shown in black triangles. The THG intensity of optical vortices exhibits a twofold polarization-dependent pattern showing the strong anisotropic nonlinear optical response, where the maximum intensity appears as the incident polarization is along the armchair axis and the minimum intensity occurs for the polarization along the zigzag axis. The measured anisotropy ratio of TH optical vortices defined as the ratio of the maximum intensity to the minimum one is 7.03 which is higher than the value of 3.57 for the bare flake due to the contamination by gallium ions during the FIB milling process. The solid curves in Figure 2g represent the theoretical fittings using Equation (1), indicating the good agreement with the measured data.

Next, the effect of the relative orientation of the grating lines in fork hologram with respect to the armchair axis on the anisotropic responses of the generated TH optical vortices is studied. According to Equation (1), the maximum THG intensity is expected to occur for the incident linear polarization along the armchair direction, which is independent of the orientation of the fork hologram. **Figure** 3a,b shows the optical image and SEM image of the fabricated fork hologram with the grating lines having ≈45° angle to the armchair axis. From the AFM image shown in Figure 3c, the GeAs flake has the thickness of around 80 nm. The TH image of the hologram and the far-field Fourier space image of the generated TH optical vortices are shown in Figure 3d,e, respectively. Figure 3f further verifies TC = ±1 for the optical vortices through the cylindrical lens transformation. Polarization angle dependence of the THG intensity of the generated optical vortices is plotted in Figure 3g, showing a twofold pattern with the maximum intensity occurring for the incident polarization along the armchair axis. The measured anisotropy ratio of TH optical vortices is 2.81 which is less than the value of 6.19 for the bare flake itself attributed to the FIB milling process. The measurements are further repeated for a fork hologram fabricated with the grating lines at 90° angle to the armchair axis. Like the cases of 0° and 45° oriented holograms, the 90° oriented hologram is also expected to generate the maximum THG intensity for the incident polarization along the armchair direction. The optical image and SEM image of the fabricated hologram are shown in **Figure** 4a,b. The AFM image in Figure 4c gives the flake thickness of around 75 nm. Figure 4d–f displays the TH image of the hologram, the far-field TH image and the cylindrical lens transformed image of the generated optical vortices with TC = ±1, respectively. Like the anisotropic TH vortex beams observed for the 0° and 45° oriented holograms, the polarization dependence of the 90° oriented hologram also exhibits a two-lobe profile as plotted in Figure 4g. Again, the maximum THG intensity of the optical vortices are found when the incident polarization is along the armchair axis. The measured

© 2025 Wiley-VCH GmbH

18638899, 2025, 7, Downloaded from https://onlinelibrary.wiley.com/doi/10.1002/lpor.202401519 by Stony Brook University Libraries, Wiley Online Library on [02/07/2025]. See the Terms and Conditions (https://onlinelibrary.wiley.com/terms-and-conditions) on Wiley Online Library for rules of use; OA articles are governed by the applicable Creative Commons License

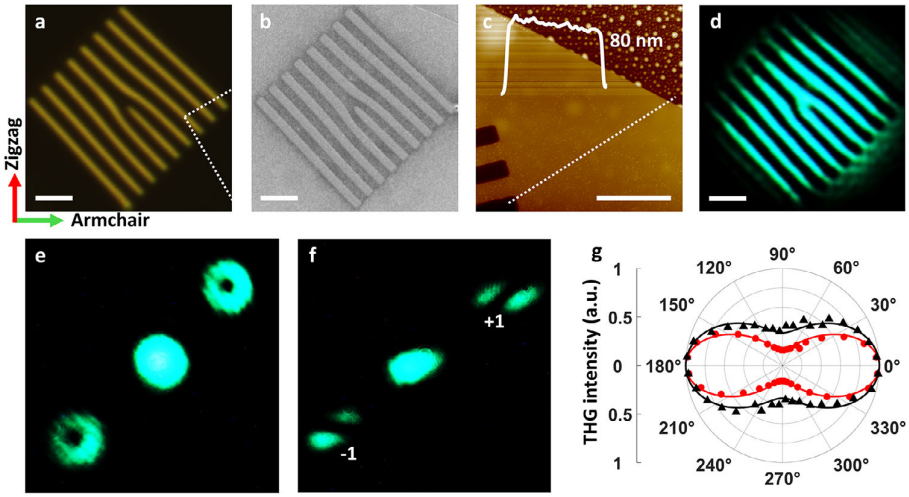

Figure 3. Anisotropic TH vortex generation with TC = ±1 with the grating lines oriented at 45° to the armchair axis. a) Optical image, b) SEM image, and c) AFM image of the hologram. d) TH image of the hologram. All scale bars are 5 μm. e) Far-field TH image of the hologram. f) Cylindrical lens transformed image. g) Polarization angle dependence of the THG intensity of optical vortices (black triangles) and the THG intensity from the bare flake (red dots). Solid curves are the corresponding theoretical fittings.

anisotropy ratio of optical vortices is 7.19 which is similar to the value of 6.01 for the bare flake. The above measurements with the fork holograms oriented along different directions with respect to the armchair axis demonstrate the versatility of the devices considered here and predict highly anisotropic TH vortex beam generation having twofold polarization dependence pattern with the maximum THG intensity occurring along the armchair axis for an arbitrarily oriented fork hologram.

The THG conversion efficiency of the hologram η_{CE} is defined as the ratio of the THG power at the output and the excitation pump power. The THG conversion efficiency is measured by setting the incident linear polarization of pump beam along the armchair direction. The average pump power in the measurements is 56 mW which corresponds to a peak irradiance of 1.36 GW cm^{-2}. The THG power is integrated from the charge-coupled device (CCD) image of THG emission from the fork grating. The THG conversion efficiencies are determined as 3.13×10^{-10}, 2.29×10^{-10}, and 2.27×10^{-10} for the 0°, 45°, and 90° oriented fork grating holograms, respectively. It is shown that the THG conversion efficiencies are almost the same for the 0°, 45°, and 90° oriented fork gratings with the flake thicknesses of 90, 80, and 75 nm, respectively. This result is consistent with the previously demonstrated optimal GeAs flake thickness range between 40 and 120 nm in terms of high THG conversion efficiency.[47]

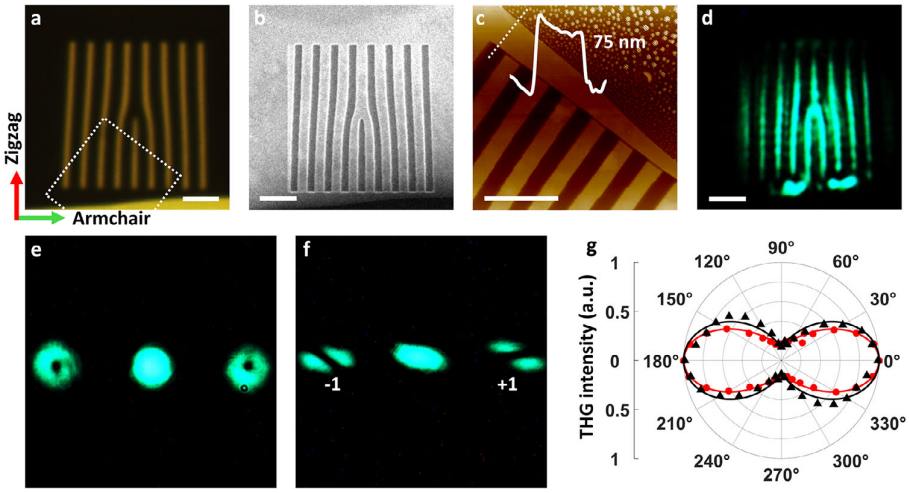

Figure 4. Anisotropic TH vortex generation with TC = ±1 with the grating lines oriented at 90° to the armchair axis. a) Optical image, b) SEM image, and c) AFM image of the hologram. d) TH image of the hologram. All scale bars are 5 μm. e) Far-field TH image of the hologram. f) Cylindrical lens transformed image. g) Polarization angle dependence of the THG intensity of optical vortices (black triangles) and the THG intensity from the bare flake (red dots). Solid curves are the corresponding theoretical fittings.

© 2025 Wiley-VCH GmbH

18638899, 2025, 7, Downloaded from https://onlinelibrary.wiley.com/doi/10.1002/lpor.202401519 by Stony Brook University Libraries, Wiley Online Library on [02/07/2025]. See the Terms and Conditions (https://onlinelibrary.wiley.com/terms-and-conditions) on Wiley Online Library for rules of use; OA articles are governed by the applicable Creative Commons License

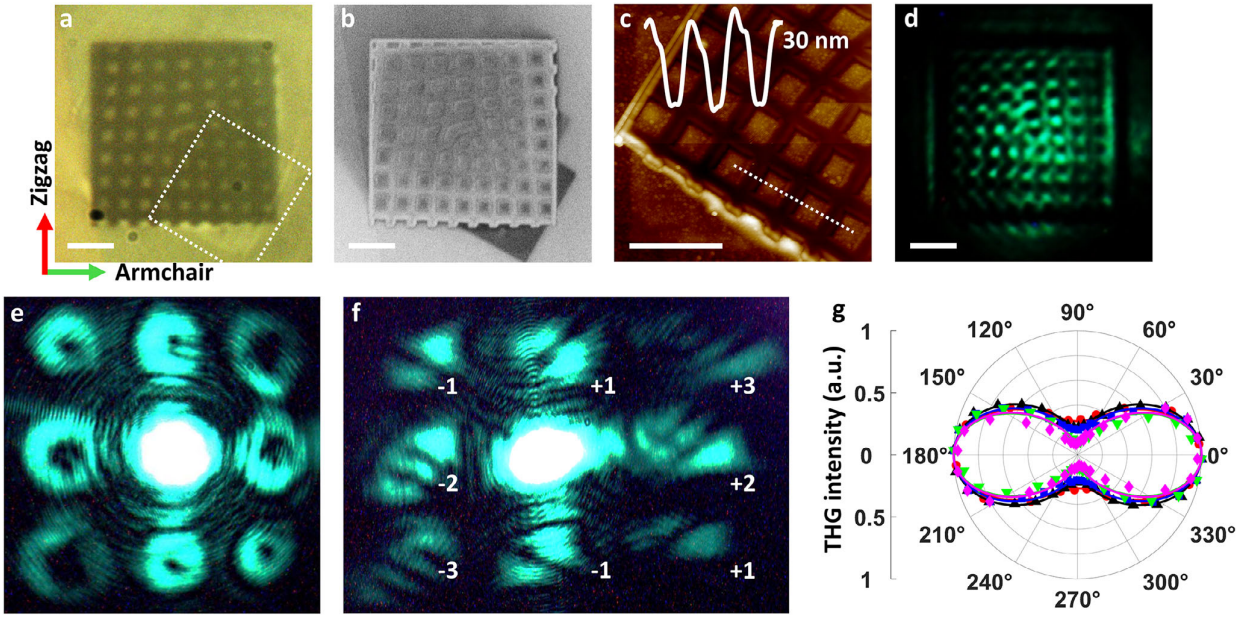

Figure 5. Generation of multiple TH optical vortices of different TCs using a 2D fork hologram with $l_x = 2$ and $l_y = 1$. a) Optical image, b) SEM image, and c) AFM image of the hologram. d) TH image of the hologram with 1560 nm excitation. All scale bars are 5 μm. e) Far-field TH image of the hologram showing the generation of multiple vortex beams in the first diffraction orders. f) Cylindrical lens transformed image illustrating the TCs of optical vortices. g) Polarization angle dependence of the THG intensity from the bare flake (red dots) and the THG intensity of optical vortices. The measured data for the optical vortices with TCs of ±2 (*x* oriented), ±1 (*y* oriented), ±1 (left diagonal), and ±3 (right diagonal) are represented by blue squares, black triangles, magenta diamonds, and green triangles, respectively. Solid curves are the corresponding theoretical fittings.

The TH vortex conversion efficiency η_{vortex} for the generated TH vortices at the first diffraction order is defined as the fraction of the excitation pump power converted into the first-order TH vortices at the output with $\eta_{vortex} = \eta_{CE}.\eta_{DE}$, where η_{DE} represents the diffraction efficiency defined as the fraction of THG power coupled to the first diffraction order. The diffraction efficiencies for the first diffraction order are calculated as 30.5%, 24.5%, and 26.0% for the 0°, 45°, and 90° oriented fork gratings, respectively. Finally, the TH vortex conversion efficiencies for the three fork gratings are determined as 9.53×10^{-11}, 5.60×10^{-11}, and 5.90×10^{-11}, respectively.

Furthermore, the demonstrated 1D fork holograms to produce anisotropic TH optical vortex beam with a defined topological charge is further extended to a 2D fork hologram to generate multiple optical vortices of different topological charges with strong anisotropic responses. Binary amplitude modulations of the third-order nonlinear susceptibility are performed along both in-plane orthogonal directions of *x* and *y* axes to obtain the 2D fork hologram, which is described as the product of two fork grating functions in Equation (2) with $\chi^{(3)}_{2D}(x, y) = \chi^{(3)}_{l_x}(x, y) \cdot \chi^{(3)}_{l_y}(y, x)$. The constructed 2D fork hologram allows independent control over the TCs of the generated TH optical vortices in each direction, with TC = l_x in the *x* direction and TC = l_y in the *y* direction. **Figure 5**a,b shows the optical image and SEM image of the FIB milled 2D fork hologram with $l_x = 2$ and $l_y = 1$. The corresponding AFM image plotted in Figure 5c indicates that the thickness of the GeAs flake is ≈30 nm. The TH image of the fabricated 2D fork hologram under the excitation at 1560 nm is shown in Figure 5d. The far-field Fourier space TH image of the hologram is displayed in Figure 5e, showing multiple optical vortices distributed in a square lattice are produced through coherent diffraction from the hologram. It is observed that the ring radius of vortex intensity profile varies, indicating different TCs for the generated optical vortices. The 2D fork hologram produces the TH optical vortices with TC = ±2 along the *x* axis and TC = ±1 along the *y* axis in the first diffraction order with the diffraction angles of 12.6°. Additionally, another two sets of TH optical vortices are generated with TC = ±1 along the left diagonal direction and TC = ±3 along the right diagonal direction with the diffraction angles of 18.1°, due to the destructive and constructive interference of vortex beams, respectively. Cylindrical lens transformed image of all these optical vortices is shown in Figure 5f, which confirms the TCs of the generated optical vortices. Next, the polarization dependence of the THG intensity for each set of optical vortices is studied separately to show the anisotropic responses, which are summarized in Figure 5g. All four sets of optical vortices show the two-lobe polarization dependence profiles with the THG intensity maxima occurring along the armchair axis. The measured anisotropy ratios for the four sets of vortices are 4.91 for TC = ±2 along the *x* axis, 4.51 for TC = ±1 along the *y* axis, 9.22 for TC = ±1 along the left diagonal direction, and 11.15 for TC = ±3 along the right diagonal direction, which are higher than the value of 3.44 for the bare flake. The above results demonstrate that a single 2D fork hologram can be used to generate eight TH optical vortices with different TCs. While the TCs of the *x*- and *y*-oriented optical vortices can be independently controlled by setting the values of l_x and l_y, the

© 2025 Wiley-VCH GmbH

18638899, 2025, 7, Downloaded from https://onlinelibrary.wiley.com/doi/10.1002/lpor.202401519 by Stony Brook University Libraries, Wiley Online Library on [02/07/2025]. See the Terms and Conditions (https://onlinelibrary.wiley.com/terms-and-conditions) on Wiley Online Library for rules of use; OA articles are governed by the applicable Creative Commons License

Table 1. Comparison of the retrieved relative magnitudes of third-order nonlinear susceptibility elements of GeAs crystal and the measured THG anisotropy ratio for the bare flakes and the fabricated fork holograms.

Sample	$\chi_{11}^{(3)}$	$\chi_{18}^{(3)}$	$\chi_{22}^{(3)}$	$\chi_{29}^{(3)}$	$\lvert\chi_{11}^{(3)}\rvert^2/\lvert\chi_{22}^{(3)}\rvert^2$	Measured THG ratio
0° flake/hologram	1	0.24/0.24	0.49/0.38	0.20/0.20	4.16/6.92	3.57/7.03
45° flake/hologram	1	0.18/0.28	0.41/0.58	0.16/0.22	5.95/2.97	6.19/2.81
90° flake/hologram	1	0.18/0.26	0.42/0.40	0.16/0.22	5.67/6.25	6.01/7.19
2D flake	1	0.22	0.52	0.20	3.70	3.44
2D hologram, TC = $\pm2(x)/\pm1(y)/\pm1/\pm3$	1	0.24/0.28/0.20/0.20	0.44/0.46/0.33/0.30	0.20/0.20/0.18/0.20	5.17/4.73/ 9.18/11.11	4.91/4.51/9.22/11.15

TCs of the diagonally oriented optical vortices are determined by the addition and subtraction of OAM values of *x*- and *y*-oriented vortices.

From the theoretical fittings obtained using Equation (1), the relative magnitudes of the third-order nonlinear susceptibility elements of GeAs crystal for the bare flakes and the fabricated fork holograms can be retrieved, which are listed in **Table 1**. Particularly, the ratio of $\lvert\chi_{11}^{(3)}\rvert^2/\lvert\chi_{22}^{(3)}\rvert^2$ provides a good approximation to the THG anisotropy ratio, which varies from 2.97 to 11.11 and this fact is reflected in the variations in the fitted susceptibility terms. It is found that these theoretically fitted THG anisotropy ratios are consistent with the measured ones varying from 2.81 to 11.15 for the bare flakes and the holograms. The variations in the THG anisotropy ratio between different bare flakes can be attributed to the deformation or defects present during the mechanical exfoliation process, which have also been reported in other 2D materials.[24,47] The mechanical exfoliation process can induce additional strain inside the 2D crystal to alter the crystal structure, so that the third-order nonlinear susceptibility tensor elements can be modified. As a result, the ratio of $\lvert\chi_{11}^{(3)}\rvert^2/\lvert\chi_{22}^{(3)}\rvert^2$ can be changed between multiple exfoliations, giving rise to the variations in the THG anisotropy ratio for different exfoliated GeAs flakes. The variations in the THG anisotropy ratio between the bare flakes and the fork holograms can be attributed to the contamination of the crystal by gallium ions during the FIB milling process. The gallium ion contamination can alter the GeAs crystal structure and electronic properties, which will modify the third-order nonlinear susceptibility tensor elements and the ratio of $\lvert\chi_{11}^{(3)}\rvert^2/\lvert\chi_{22}^{(3)}\rvert^2$, so the THG anisotropy ratio for the fork grating is changed compared with the bare flake. Furthermore, the levels of gallium ion contamination in the fork gratings are different to each other due to the varying ion milling conditions used in fabrication, which will induce different levels of influence to the THG anisotropy ratio for the fork gratings. Therefore, the THG anisotropy ratio of optical vortices is different for each fork grating. Anisotropic THG of various 2D materials belonging to different crystal systems have been studied previously with the maximum reported THG anisotropy ratios of 3.24 for BP, 1.44 for ReS_2, 4.41 for GeSe, 5.76 for GeAs, 1.90 for SiP, and 2.79 for As_2S_3.[48,49] The measured THG anisotropy ratios of GeAs flakes from 3.44 to 6.19 reported here are consistent with the previously reported values for GeAs flakes with different thicknesses.[47]

3. Conclusion

In summary, we have designed and fabricated binary-amplitude fork holograms patterned on ultrathin 2D GeAs flakes to generate highly anisotropic TH optical vortex beams. It has been shown that the TH optical vortex beam with a defined topological charge can be produced with 1D fork gratings, while strong anisotropy in TH optical vortices can always be observed irrespective of the relative orientation of the fork grating lines with respect to the armchair direction of GeAs crystal. It has also been demonstrated that multiple TH optical vortices having different topological charges with strong anisotropic responses can be generated with a single 2D fork hologram. Strong anisotropic responses in the generated TH optical vortices are observed due to the low in-plane crystal symmetry of GeAs. It is demonstrated that the THG intensities of the generated optical vortices show the two-lobe polarization dependence profiles, with the maximum and minimum intensities occurring when the incident polarization is along the armchair and zigzag axes of GeAs crystal, respectively. The demonstrated binary-amplitude nonlinear hologram design based on anisotropic 2D materials can readily be extended to generate various types of exotic nonlinear optical beams by imprinting the corresponding amplitude and phase information into the 2D crystal with the binary modulation of nonlinear susceptibility. The ability to control the topological charges of nonlinear optical vortices along with having strong anisotropic responses of the 2D material-based nonlinear optical devices considered here can find potential applications in photonic integrated circuits, optical communication, and optical information processing.

4. Experimental Section

Sample Preparation: GeAs thin flakes were mechanically exfoliated from a bulk GeAs crystal (2D Semiconductors) to polydimethylsiloxane (PDMS) substrates using scotch tape and subsequently transferred to glass substrates using the dry transfer technique. Before the transfer, the glass substrates were cleaned using acetone, isopropyl alcohol, and deionized water. The fork holograms were fabricated using focused ion beam milling (FEI Helios Nanolab 600) of the GeAs flakes with the patterned area of $20 \times 20\ \mu m^2$. Before the focused ion beam patterning, the sample was spin coated with a thin layer of the water-soluble conductive polymer to avoid the surface charging built up on the sample. The polymer layer was removed by rinsing the sample with deionized water after patterning, and finally the sample was blown dry with nitrogen gas.

© 2025 Wiley-VCH GmbH

18638899, 2025, 7, Downloaded from https://onlinelibrary.wiley.com/doi/10.1002/lpor.202401519 by Stony Brook University Libraries, Wiley Online Library on [02/07/2025]. See the Terms and Conditions (https://onlinelibrary.wiley.com/terms-and-conditions) on Wiley Online Library for rules of use; OA articles are governed by the applicable Creative Commons License

Optical Setup: Linearly polarized pump laser beam at 1560 nm (Calmer fiber laser, pulse width 90 fs, repetition rate 80 MHz) was focused on the sample using a 4× objective lens (NA = 0.12). The laser spot diameter on the sample was ≈27 µm, which illuminated the entire area of the hologram. A half-wave plate was used in the excitation path to rotate the linear polarization of the pump beam. The transmitted signal from the sample was collected with a 20× objective lens (NA = 0.42), passed through a shortpass filter (900 nm) and a bandpass filter (520 nm) to select the THG emission, and imaged either in Fourier space or real space using a color CCD camera. The THG spectrum was measured with an optical spectrometer (Horiba, iHR550).

Acknowledgements

The authors acknowledge the support from the National Science Foundation under Grant Nos. ECCS-2226875 and ECCS-2226948. The authors thank the facility support from the Materials Research Center at Missouri S&T.

Conflict of Interest

The authors declare no conflict of interest.

Data Availability Statement

The data that support the findings of this study are available from the corresponding author upon reasonable request.

Keywords

2D materials, optical anisotropy, third-harmonic generation, vortex beam

Received: September 14, 2024
Revised: December 13, 2024
Published online: January 3, 2025

[1] K. Zhang, Y. Wang, Y. Yuan, S. N. Burokur, *Appl. Sci.* **2020**, *10*, 1015.
[2] N. Bozinovic, Y. Yue, Y. Ren, M. Tur, P. Kristensen, H. Huang, A. E. Willner, S. Ramachandran, *Science* **2013**, *340*, 1545.
[3] R. Fickler, R. Lapkiewicz, W. N. Plick, M. Krenn, C. Schaeff, S. Ramelow, A. Zeilinger, *Science* **2012**, *338*, 640.
[4] B. C. Hiesmayr, M. J. A. de Dood, W. Löffler, *Phys. Rev. Lett.* **2016**, *116*, 073601.
[5] X. Fang, H. Ren, M. Gu, *Nat. Photonics* **2020**, *14*, 102.
[6] M. Padgett, R. Bowman, *Nat. Photonics* **2011**, *5*, 343.
[7] M. Gecevičius, R. Drevinskas, M. Beresna, P. G. Kazansky, *Appl. Phys. Lett.* **2014**, *104*, 231110.
[8] J. Ng, Z. Lin, C. T. Chan, *Phys. Rev. Lett.* **2010**, *104*, 103601.
[9] S. N. Khonina, A. P. Porfire, N. L. Kazanskiy, *Sci. Rep.* **2020**, *10*, 5590.
[10] Y. Chen, X. Yang, J. Gao, *Adv. Opt. Mater.* **2018**, *6*, 1800646.
[11] G. Li, S. Zhang, T. Zentgraf, *Nat. Rev. Mater.* **2017**, *2*, 17010.
[12] Z. Li, W. Liu, Z. Li, C. Tang, H. Cheng, J. Li, X. Chen, S. Chen, J. Tian, *Laser Photonics Rev.* **2018**, *12*, 1800164.
[13] K. S. Novoselov, A. Mishchenko, A. Carvalho, A. H. Castro Neto, *Science* **2016**, *353*, aac9439.
[14] X. Song, Z. Guo, Q. Zhang, P. Zhou, W. Bao, D. W. Zhang, *Small* **2017**, *13*, 1700098.
[15] X. Wang, Y. Cui, T. Li, M. Lei, J. Li, Z. Wei, *Adv. Opt. Mater.* **2019**, *7*, 1801274.
[16] Z. Dai, L. Liu, Z. Zhang, *Adv. Mater.* **2019**, *31*, 1805417.
[17] H. Liu, K. Sun, X. Shi, H. Yang, H. Dong, Y. Kou, P. Das, Z. Wu, Q. Shi, *Energy Storage Mater.* **2021**, *42*, 845.
[18] G. Wang, X. Marie, I. Gerber, T. Amand, D. Lagarde, L. Bouet, M. Vidal, A. Balocchi, B. Urbaszek, *Phys. Rev. Lett.* **2015**, *114*, 097403.
[19] A. Dasgupta, J. Gao, X. Yang, *Nano Lett.* **2019**, *19*, 6511.
[20] J. J. Dean, H. M. van Driel, *Appl. Phys. Lett.* **2009**, *95*, 261910.
[21] X. Zhou, J. Cheng, Y. Zhou, T. Cao, H. Hong, Z. Liao, S. Wu, H. Peng, K. Liu, D. Yu, *J. Am. Chem. Soc.* **2015**, *137*, 7994.
[22] Y. Song, S. Hu, M. Lin, X. Gan, P. Tan, J. Zhao, *ACS Photonics* **2018**, *5*, 3485.
[23] A. Säynätjoki, L. Karvonen, J. Riikonen, W. Kim, S. Mehravar, R. A. Norwood, N. Peyghambarian, H. Lipsanen, K. Kieu, *ACS Nano* **2013**, *7*, 8441.
[24] A. Dasgupta, J. Gao, X. Yang, *Laser Photonics Rev.* **2020**, *14*, 1900416.
[25] Y. Wu, B. C. Yao, Q. Y. Feng, X. L. Cao, X. Y. Zhou, Y. J. Rao, Y. Gong, W. L. Zhang, Z. G. Wang, Y. F. Chen, K. S. Chiang, *Photon. Res.* **2015**, *3*, A64.
[26] N. Vermeulen, D. Castelló-Lurbe, J. Cheng, I. Pasternak, A. Krajewska, T. Ciuk, W. Strupinski, H. Thienpont, J. V. Erps, *Phys. Rev. Appl.* **2016**, *6*, 044006.
[27] C. Ma, C. Wang, B. Gao, J. Adams, G. Wu, H. Zhang, *Appl. Phys. Rev.* **2019**, *6*, 041304.
[28] J. W. You, S. R. Bongu, Q. Bao, N. C. Panoiu, *Nanophotonics* **2019**, *8*, 63.
[29] A. Autere, H. Jussila, Y. Dai, Y. Wang, H. Lipsanen, Z. Sun, *Adv. Mater.* **2018**, *30*, 1705963.
[30] Z. Xie, T. Zhao, X. Yu, J. Wang, *Small* **2024**, *20*, 2311621.
[31] N. Youngblood, R. Peng, A. Nemilentsau, T. Low, M. Li, *ACS Photon.* **2017**, *4*, 8.
[32] X. Zhou, X. Hu, B. Jin, J. Yu, K. Liu, H. Li, T. Zhai, *Adv. Sci.* **2018**, *5*, 1800478.
[33] H. Sar, J. Gao, X. Yang, *Sci. Rep.* **2021**, *11*, 6372.
[34] R. P. N. Tripathi, X. Yang, J. Gao, *Opt. Express* **2022**, *30*, 22661.
[35] Q. Cui, R. A. Muniz, J. E. Sipe, H. Zhao, *Phys. Rev. B* **2017**, *95*, 165406.
[36] R. Biswas, M. Dandu, S. Menon, K. K. Jha, K. M. Jyothsna, K. Majumdar, V. Raghunathan, *Opt. Express* **2019**, *27*, 28855.
[37] H. Yuan, X. Liu, F. Afshinmanesh, W. Li, G. Xu, J. Sun, B. Lian, A. G. Curto, G. Ye, Y. Hikita, Z. Shen, S. Zhang, X. Chen, M. Brongersma, H. Y. Hwang, Y. Cui, *Nat. Nanotechnol.* **2015**, *10*, 707.
[38] C. Tan, P. Yu, Y. Hu, J. Chen, Y. Huang, Y. Cai, Z. Luo, B. Li, Q. Lu, L. Wang, Z. Liu, H. Zhang, *J. Am. Chem. Soc.* **2015**, *137*, 10430.
[39] D. Li, H. Jussila, L. Karvonen, G. Ye, H. Lipsanen, X. Chen, Z. Sun, *Sci. Rep.* **2015**, *5*, 15899.
[40] Q. Hong, W. Xu, J. Zhang, Z. Zhu, X. Yuan, S. Qin, *Opt. Lett.* **2019**, *44*, 1774.
[41] H. Yang, H. Jussila, A. Autere, H. Komsa, G. Ye, X. Chen, T. Hasan, Z. Sun, *ACS Photonics* **2017**, *4*, 3023.
[42] E. Liu, Y. Fu, Y. Wang, Y. Feng, H. Liu, X. Wan, W. Zhou, B. Wang, L. Shao, C. Ho, Y. Huang, Z. Cao, L. Wang, A. Li, J. Zeng, F. Song, X. Wang, Y. Shi, H. Yuan, H. Y. Hwang, Y. Cui, F. Miao, D. Xing, *Nat. Commun.* **2015**, *6*, 6991.
[43] H. Wang, M. Chen, M. Zhu, Y. Wang, B. Dong, X. Sun, X. Zhang, S. Cao, X. Li, J. Huang, L. Zhang, W. Liu, D. Sun, Y. Ye, K. Song, J. Wang, Y. Han, T. Yang, H. Guo, C. Qin, L. Xiao, J. Zhang, J. Chen, Z. Han, Z. Zhang, *Nat. Commun.* **2019**, *10*, 2302.
[44] J. Guo, Y. Liu, Y. Ma, E. Zhu, S. Lee, Z. Lu, Z. Zhao, C. Xu, S. Lee, H. Wu, K. Kovnir, Y. Huang, X. Duan, *Adv. Mater.* **2018**, *30*, 1705934.
[45] K. Lee, S. Kamali, T. Ericsson, M. Bellard, K. Kovnir, *Chem. Mater.* **2016**, *28*, 2776.
[46] L. Liu, V. V. Struzhkin, J. Ying, *Phys. Rev. B.* **2019**, *100*, 214516.
[47] H. Sar, J. Gao, X. Yang, *Sci. Rep.* **2020**, *10*, 14282.
[48] A. Dasgupta, X. Yang, J. Gao, *npj 2D Mater. Appl.* **2021**, *5*, 74.
[49] A. Dasgupta, D. I. Belakovskiy, I. V. Chaplygin, J. Gao, X. Yang, *Sci. Rep.* **2022**, *12*, 16803.

© 2025 Wiley-VCH GmbH

18638899, 2025, 7, Downloaded from https://onlinelibrary.wiley.com/doi/10.1002/lpor.202401519 by Stony Brook University Libraries, Wiley Online Library on [02/07/2025]. See the Terms and Conditions (https://onlinelibrary.wiley.com/terms-and-conditions) on Wiley Online Library for rules of use; OA articles are governed by the applicable Creative Commons License